



Numerical study of the parameters governing the impact dynamics of yield-stress fluid droplets on a solid surface

Eunjeong Kim, Jehyun Baek^{*}

Department of Mechanical Engineering, POSTECH, San 31, Hyoja-dong, Pohang 790-784, Republic of Korea

ARTICLE INFO

Article history:

Received 8 November 2011

Received in revised form 27 February 2012

Accepted 27 February 2012

Available online 6 March 2012

Keywords:

Yield-stress fluids

Droplet impact

Volume of fluid model

ABSTRACT

The impact dynamics of a droplet onto a solid surface are important in a variety of applications, such as inkjet printing and spray coating. Many fluids encountered in practical industrial applications exhibit non-Newtonian behavior, and therefore more research associated with non-Newtonian fluids is necessary. This paper reports on a numerical study of the impact dynamics of yield-stress fluid droplets. The numerical simulation is performed using a computational fluid dynamics package, Fluent 6.3, with a volume of fluid model. The numerical simulation models the presence of yield-stress and shear-rate dependent viscosity using the Herschel–Bulkley rheological model. The numerical results are found to be in qualitative agreement with experimental data in the literature. By performing extensive numerical simulations varying the impact velocity, rheological parameters, and surface tension, the influence of these parameters on the impact dynamics are evaluated, and the dominant effects that govern the spreading and relaxation phases are determined. The results show that while the spreading behavior is determined by the power-law index n , the non-Newtonian Reynolds number Re_n , and the Weber number We , the retraction behavior is determined by the non-Newtonian capillary Ca_n and the Bingham–capillary number \hat{B} . In addition, the scaling law that predicts the maximum spreading diameter is presented.

© 2012 Elsevier B.V. All rights reserved.

1. Introduction

The impact dynamics of a droplet onto a solid surface is of fundamental importance in a variety of applications, such as inkjet printing and spray coating, and has been studied for over a century. When a droplet impacts onto solid surfaces, the impact process can be divided into four phases: the kinematic, spreading, relaxation, and equilibrium phases [1]. At the early stage after the impact, namely, the kinematic phase, a droplet spreads without visible lamella. In the spreading phase, the flow is driven radially outward at the base of the droplet. The spreading phase continues until the maximum spread is attained. In the relaxation phase, the droplet retracts on the partially wetting surface or continuously spreads on the completely wetting surface. Finally, in the equilibrium phase, the droplet reaches a final sessile state.

Much of the previous work in the field of droplet impacts concerns Newtonian fluids [1–14]. However, many fluids encountered in industrial applications exhibit complex non-Newtonian behavior. In this study, we focused on a particular non-Newtonian fluid type known as a yield-stress fluid. A yield-stress fluid flows at shear stresses higher than the yield stress, but behaves as a rigid solid at shear stresses below the yield stress. Some yield-stress fluids exhibit shear-thinning behavior, in which the viscosity

decreases with increasing shear rate. An example of the application of a yield-stress fluid is in direct ink writing of complex 3D structures, where colloidal gels, which exhibit the rheological properties of yield-stress fluids, are excellent candidate materials [15]. An understanding of the impact and spreading dynamics of a yield-stress fluid droplet, as used in such applications, is challenging and requires further investigation.

Recently, the impact dynamics of yield-stress fluid droplets have been studied experimentally. Nigen [16] first examined the droplet impact of a yield-stress fluid with various impact velocities. At relatively low impact velocities, a two stage impact process was observed: the inertial spreading, and subsequent slow spreading induced by gravity. At relatively high impact velocities, retraction did not occur because the surface tension was insufficient to overcome the yield stress. Luu and Forterre [17] investigated the impact of yield-stress fluid droplets (clay suspension, Carbopol gel) onto different solid surfaces (partially wetting, super-hydrophobic). They observed no retraction after the maximum spreading for clay suspensions, irrespective of its wetting property. By contrast, retraction was observed in the Carbopol gel on the super-hydrophobic surfaces. In addition, they suggested a scaling law, which predicts the maximum spreading diameter as a function of a non-dimensional parameter. German and Bertola [18] compared the impact behavior of purely shear-thinning fluid and yield-stress fluid droplets with that of Newtonian droplets. In their work, yield-stress fluid droplets exhibited central droplet peaks at the end of

^{*} Corresponding author. Tel.: +82 54 2792168; fax: +82 54 2793199.

E-mail address: jhbaek@postech.ac.kr (J. Baek).

the inertial spreading. The impact morphology of the purely shear-thinning fluids turned out to be qualitatively similar to that of Newtonian fluids. In a subsequent paper [19], they distinguished capillary-governed and viscoplastic-governed regimes based on the Bingham–Capillary number, which is defined as the ratio of yield-stress to capillary pressure. In the capillary-governed regime corresponding to a low Bingham–Capillary number, the contact angles at equilibrium remained nearly identical, irrespective of the yield-stress magnitude and impact velocity. In the viscoplastic-governed regime corresponding to a high Bingham–Capillary number, the contact angles at equilibrium varied with the yield-stress magnitude and impact velocity, indicating that the equilibrium conditions were not only governed by capillary forces, but also by intrinsic rheological properties. Saïdi et al. [20] studied the impact of yield-stress fluid droplets using a solution of Carbopol gel. Droplets were impacted across a wide range of yield-stress magnitudes and velocities. They found that an increase in the gel concentration weakened both the spreading and the retraction. They also observed that a yield-stress fluid droplet converges to a different equilibrium state depending on the impact velocity, while water droplets converge to the same equilibrium state irrespective of impact velocity.

In practice, many parameters affect the impact dynamics of yield-stress fluid droplets. Thus, we employed a numerical method in order to evaluate the influence of various parameters systematically. Numerical simulations also have the advantage of obtaining a detailed description of the transient flow field, which is useful for analysis of the impact dynamics. Prior to examining the droplet impact behavior as a function of the various parameters, the numerical results were compared with the experimental results of Saïdi et al. [20].

In this study, we focused on the determination of non-dimensional parameters that govern the impact dynamics of yield-stress fluid droplets. Typically, the droplet impact behavior of Newtonian fluids can be characterized by non-dimensional parameters such as the Reynolds number Re , the Weber number We , and the capillary number Ca [18,21]. However, rheological features of a yield-stress fluid, such as additional plastic-like dissipation by yield-stress and shear-rate dependent viscosity [17], induce different droplet impact hydrodynamics than in Newtonian fluids, and therefore the implementation of these non-dimensional parameters is not possible for characterizing the impact behavior of a yield-stress fluid droplet. Therefore, we attempted to characterize the impact dynamics of yield-stress fluid droplets in terms of non-dimensional parameters accounting for rheological features. Prior to characterizing the impact dynamics, extensive numerical simulations were performed by varying the impact velocity, rheological parameters, and surface tension, and the influence of these parameters on the impact dynamics were evaluated. The spread and retraction behavior was described in terms of the temporal variation of the base diameter of a droplet on the solid surface. Furthermore, we attempted to predict the maximum spreading diameter as a function of non-dimensional parameters. The numerical study considered only deposition situations, and splashing or rebounding was absent under the range of impact conditions studied herein.

2. Numerical methods

2.1. A rheological model of yield-stress fluid and non-dimensional parameters

Yield-stress fluids do not exhibit noticeable viscoelastic effects [22]. Inelastic-viscoplastic rheological features can be represented using the Herschel–Bulkley model, given by

$$\dot{\gamma} = 0 \quad \text{for } \tau < \tau_0, \quad (1)$$

$$\tau = \tau_0 + K\dot{\gamma}^n \quad \text{for } \tau > \tau_0, \quad (2)$$

where $\dot{\gamma}$ is the shear rate (s^{-1}), and τ is the shear stress (Pa). In Eq. (2), τ_0 , K , and n are rheological parameters that represent the yield-stress magnitude (Pa), the consistency factor ($Pa\ s^n$), and the power-law index, respectively. An increase in τ_0 induces an increase in additional plastic-like dissipation, and an increase in K increases the apparent viscosity. The power-law index n is related to the shear-thinning behavior—as n decreases, the fluid becomes more shear-thinning. The first and last terms in the right-hand side of Eq. (2) are relevant to yield-stress effects and viscous effects, respectively.

In numerical modeling of the Herschel–Bulkley model, regularized formulation is needed to overcome the issues relevant to discontinuous material behavior. Burgos and Alexandrou [30] compared some regularized formulations of the Herschel–Bulkley model. They found that the Papanastasiou model predicts well the yield surface ($\tau = \tau_0$), while both the Papanastasiou model and the bi-viscosity model proposed by O'Donovan and Tanner [29] predicts well the stress field away from $\tau = \tau_0$. In this study, we employed the bi-viscosity model based on the assumption that the stress field during the droplet impact is away from $\tau = \tau_0$. In practice, the unyielded region (solid-like) is described by Eq. (1), but is numerically defined by $\dot{\gamma} < \dot{\gamma}_0$ rather than by $\dot{\gamma} = 0$. The value of $\dot{\gamma}_0$ must be sufficiently small to obtain an accurate estimate in the unyielded zone. The $\dot{\gamma}_0$ criterion for an accurate prediction is defined as follows [24]:

$$\dot{\gamma}_0 \leq \left(\frac{\tau_0}{999K} \right)^{1/n}. \quad (3)$$

In the unyielded region, the rigid material acts as a very viscous fluid with a yielding viscosity of $\mu_0 = \tau_0/\dot{\gamma}_0$. The model used to describe the fluid behavior in the numerical simulation is given by

$$\mu = \frac{\tau_0 + K[\dot{\gamma}^n - (\tau_0/\mu_0)^n]}{\dot{\gamma}}. \quad (4)$$

However, the numerical results showed that the stress field during the droplet impact was away from $\tau = \tau_0$, therefore the value of $\dot{\gamma}_0$, which determines the boundary between the unyielded and yielded region, had no significant effect on the numerical results.

In this study, discussed are the effects of various parameters on the impact dynamics of yield-stress fluid droplets in terms of non-dimensional parameters, such as the non-Newtonian Reynolds number Re_n , the Weber number We , the Bond number Bo , and a new non-dimensional parameter introduced by Bertola [31] such as the Bingham-capillary number. These parameters are defined as follows:

$$Re_n = \frac{\text{Inertial effects}}{\text{Viscous effects}} = \frac{\rho D_0^n V_0^{2-n}}{K}, \quad (5)$$

$$We = \frac{\text{Inertial effects}}{\text{Capillary effects}} = \frac{\rho V_0^2 D_0}{\sigma}, \quad (6)$$

$$Bo = \frac{\text{Gravity effects}}{\text{Capillary effects}} = \frac{\rho g D_0^2}{\sigma}, \quad (7)$$

$$\hat{B} = \frac{\text{Yield stress effects}}{\text{Capillary effects}} = \frac{D_0 \tau_0}{\sigma}, \quad (8)$$

where D_0 is the initial droplet diameter (m), V_0 is the impact velocity ($m\ s^{-1}$), σ is the surface tension ($N\ m^{-1}$), and ρ is the density ($kg\ m^{-3}$). Other relevant non-dimensional parameters are the non-Newtonian capillary number $Ca_n = We/Re_n$ and the Bingham

number $Bi = \hat{B}/Ca_n$ which represent the ratios of viscous to capillary and yield stress to viscous effects, respectively.

2.2. Governing equations

In this study, the droplet impact dynamics were considered to be axisymmetric. The numerical simulation of two-dimensional axisymmetric, transient, incompressible, laminar, two-phase flow was performed using a commercial CFD package, Fluent 6.3. The time-dependent governing equations for the continuity and momentum were

$$\frac{\partial \rho}{\partial t} + \nabla \cdot (\rho \vec{v}) = 0, \quad (9)$$

$$\frac{\partial}{\partial t}(\rho \vec{v}) + \nabla \cdot (\rho \vec{v} \vec{v}) = -\nabla p + \nabla \cdot [\mu(\nabla \vec{v} + \nabla \vec{v}^T)] + \rho \vec{g} + \vec{F}, \quad (10)$$

where \vec{v} is the velocity vector, p is the pressure, \vec{g} is the gravitational acceleration, μ is the viscosity, and \vec{F} is the surface tension force per unit volume.

The volume of fluid (VOF) model [25] was used to track the gas–liquid interface by solving the volume fraction equation, given by

$$\frac{\partial \alpha_G}{\partial t} + \vec{v} \cdot \alpha_G = 0, \quad (11)$$

where α_G is the volume fraction of the gas in a computational cell. $\alpha_G = 1$ indicates that the computational cell is completely filled with gas, while $\alpha_G = 0$ indicates that the cell is completely filled with liquid. The gas–liquid interface exists in cells where $0 < \alpha_G < 1$.

The density and viscosity in the VOF model are given by

$$\rho = \alpha_G \rho_G + (1 - \alpha_G) \rho_L, \quad (12)$$

$$\mu = \alpha_G \mu_G + (1 - \alpha_G) \mu_L. \quad (13)$$

The subscripts G and L represent the gas and liquid phases, respectively. The surface tension force \vec{F} in Eq. (12) was modeled using the continuum surface force (CSF) model [26] as follows:

$$\vec{F} = \sigma \frac{\rho \kappa \nabla \alpha_G}{\frac{1}{2}(\rho_L + \rho_G)}, \quad (14)$$

where κ is the curvature of the gas–liquid interface, calculated as $\kappa = -(\nabla \cdot \hat{n})$,

and the unit vector \hat{n} normal to the interface is given by

$$\hat{n} = \frac{\nabla \alpha_G}{|\nabla \alpha_G|}. \quad (16)$$

In order to account for wall adhesion effects, the unit normal to the interface at the cell next to the wall boundary was calculated using the contact angle θ , which represents the wetting properties of the wall and is defined as the angle between the wall and the tangent to the interface at the wall, measured inside the liquid phase, as follows:

$$\hat{n} = \hat{n}_w \cos \theta + \hat{t}_w \sin \theta, \quad (17)$$

where \hat{n}_w and \hat{t}_w are the unit vectors normal and tangential to the wall, respectively.

The pressure implicit with splitting of operators (PISOs) scheme was used for the pressure–velocity coupling, as it reduces the number of iterations required for convergence, especially in unsteady systems. A pressure staggering option (PRESTO!) scheme and second-order upwind scheme were used to interpolate the pressure and momentum equations, respectively. The compressive interface capturing scheme for arbitrary meshes (CICSAMs) was used for interface reconstruction, as this scheme is particularly suitable for flows with high viscosity ratios between phases. A variable time

stepping method, in which the time step was calculated for a fixed value of the Courant number (0.2), was used to reduce the calculation time.

2.3. Boundary conditions

A schematic illustration of the computational domain and boundary conditions is shown in Fig. 1. The radius and height of the cylindrical computational domains are $4D_0$ and $3D_0$, respectively. A no-slip condition was imposed on the substrate; however, the VOF method introduced an implicit slip length of the order of the grid spacing. The fluid was described by the following values: density $\rho = 1000 \text{ kg m}^{-3}$, surface tension $\sigma = 0.071 \text{ N m}^{-1}$ (unless mentioned otherwise), and initial diameter $D_0 = 2 \text{ mm}$ of the droplet. Although a much larger droplet than that in practical applications such as ink jet printing was used in the numerical simulations, the Reynolds and Weber number were in the typical range of Re and We for ink jet printing ($O(10) < Re < O(10^3)$, $O(1) < We < O(10^2)$) [37]. According to Dong et al. [38], micron and millimeter droplets at the same dimensionless number show similar impaction behavior except that spreading diameter of millimeter droplets is usually slightly larger due to the larger effect of gravity on the millimeter droplet impaction. Therefore, the numerical results despite at the larger scale could provide useful information for the actual process. The initial shape was spherical. Gravity effects were neglected in the numerical simulations because the droplet radius ($D_0/2$) was smaller than the capillary length $a = \sqrt{\sigma/\rho g}$, below which gravity is not a dominant effect.

An appropriate dynamic contact angle model is important to accurately describe the droplet impact process. The dynamic contact angle is known as it depends on the contact line velocity. However, the precise relationship between contact line velocity and contact angle is not fully understood. Many researchers have been used simplified model of a constant advancing and receding contact angle as input boundary conditions for their numerical models [34–36] and obtained reasonable results. In our numerical simulations for comparison with experimental data [20], we used a constant advancing and receding contact angle during spreading and retraction, respectively. The dynamic contact angle for very viscous materials such as viscoplastic fluid was found to be between 160° and 180° [32,33]. For the comparison with experimental results of Saïdi et al. [20], the value of advancing contact angle between 170° and 175° was given. The receding contact angle was assumed to be an equilibrium angle of 81° [20]. Except the simulation cases for comparison with experiments, a static contact angle model was used with a constant value of 90° . Although a static contact angle model may not be realistic because the spreading contact angle

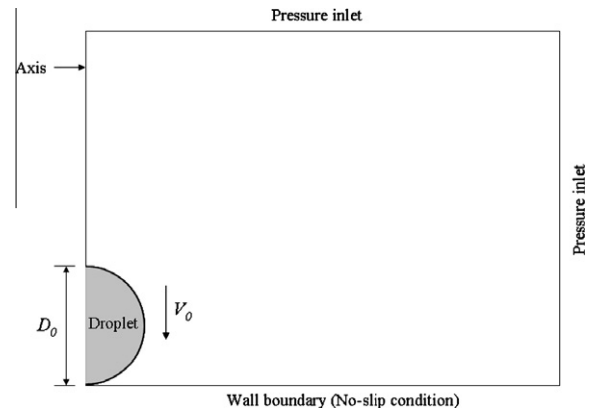


Fig. 1. Schematic diagram showing the computational domain and boundary conditions.

and the recoiling contact angle are different, it is believed that the numerical results could provide qualitative evaluation on the effects of various parameters.

3. Results and discussion

3.1. Comparison of the numerical results with experimental results and generic features of the impact process

Prior to the detailed discussion on the droplet impact dynamics, numerical results in terms of the spreading parameter (D/D_0) were compared with experimental data of Saïdi et al. [20], where D is the contact diameter on a substrate and D_0 the initial droplet diameter. In the experiments, a solution of Carbopol gel was used as a yield-stress fluid, and the magnitude of the yield-stress was controlled by varying the weight concentration of gel in the solution. They conducted droplet impact experiments onto a polymethylmethacrylate (PMMA) surface over a wide range of impact velocities between 0.3 and 3.0 m s⁻¹.

For the verification of the computation, numerical simulations of droplet impact were performed with appropriate impact conditions for the experiments of Saïdi et al. [20], considering that the initial droplet does not display a prolate shape and wall slip effects do not appear during the impact process. Wall slip effects, which can induce apparent fluid motion below the yield-stress, did not significantly influence the impact process unless the droplet had a very low impact velocity [23]. The selected experiments set are listed in Table 1.

In order to understand the effect of grid size on the numerical results, three grid sizes of 40, 80, and 160 cells per initial droplet diameter were considered. The numerical simulations for case 1 using grid systems of $D_0/80$ and $D_0/160$ were compared with that of using a grid system of $D_0/40$ during the spreading phase, revealing that the calculated spreading parameters did not vary significantly as shown in the inset of Fig. 2a. Therefore, all further simulations were performed using a $D_0/40$ grid system.

The spreading parameters obtained numerically were compared with those of experiments as shown in Fig. 2. The numerical simulations showed the overpredicted maximum spreading parameter with relative errors of 13%, 7%, and 16.5% for validation cases 1, 2, and 4, respectively. In case 3, the maximum spreading parameter agreed well with the experimental results. Discrepancies between the experimental and numerical results during the spreading phase may be attributed to parasitic currents (unphysical currents) generated in fluid regions adjacent to an interface by local variations in the CSF body force [40]. While the parasitic currents do not affect the fluid viscosity for Newtonian droplet impact, it seems that parasitic currents make shear rate overestimated for the yield-stress fluid in the region adjacent to an interface, resulting in the underestimated apparent viscosity due to shear-thinning behavior. As a result of underestimated viscosity near the contact line, it seems that thinner lamella comes out at the droplet base, resulting in the faster radial flow in the lamella and larger maximum spreading diameter than those in the real physics. Therefore, it is numerically challenging problem to reduce the effect of parasitic currents on the impact dynamics of non-Newtonian droplet. Popinet [41] developed the Gerris solver, where the balanced-force scheme for the CSF model and height function methodology for the interface

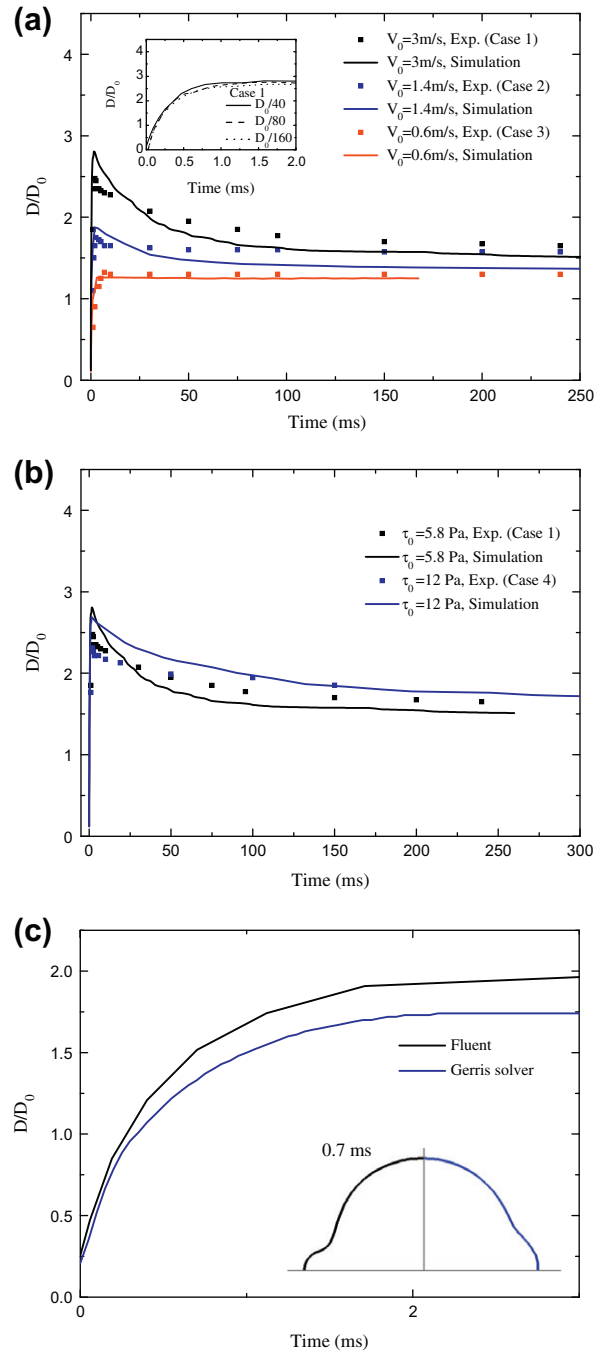


Fig. 2. Comparison of the numerical results with the experiments of Saïdi et al. [20]. (a) Influence of impact velocity with identical rheological parameters. (b) Influence of rheological properties at identical impact velocity. (c) Comparison of the numerical results using Fluent and Gerris solver. The computational domain and mesh were $3D_0 \times 3D_0$ and 128×128 , respectively. The left and right side of inset figure are the results of Fluent and Gerris solver at 0.7 ms.

curvature estimation were implemented, and parasitic currents around a stationary droplet was eliminated. In order to find the

Table 1

Experiments set [20] for the comparison of the numerical results with experimental results.

	τ_0 (Pa)	K (Pa s ⁿ)	n	Impact velocity (m/s)	Grid resolution
Case 1	5.8	3	0.42	3	$D_0/40$, $D_0/80$, $D_0/160$
Case 2	5.8	3	0.42	1.4	$D_0/40$
Case 3	5.8	3	0.42	0.6	$D_0/40$
Case 4	12	5.5	0.38	3	$D_0/40$

cause of discrepancy, Gerris solver was first applied to a stationary droplet test with Gel 3. The numerical results showed that parasitic currents and shear rate near the interface were approximately two orders of magnitude lower than those of Fluent's results. This indicates that parasitic currents influenced on the shear rate and consequently apparent viscosity of non-Newtonian droplet, and could be reduced by using accurate numerical method, Gerris solver. Then, the numerical simulations of droplet impact for Gel 3, $V_0 = 1$ m/s and static contact angle condition of 90° were performed using Fluent and Gerris solver. As shown in Fig. 2c, the spreading rate using Fluent was faster than that using Gerris solver, indicating that parasitic currents affect the numerical results in such a manner that it makes apparent viscosity underestimated, lamella thinner and consequently spreading rate overestimated. On the other hand, in the equilibrium phase, the numerical results tend to underpredict the spreading parameter. This discrepancy may be attributed to the use of an inaccurate equilibrium contact angle (81°), which was obtained for a water droplet on a PMMA surface [20]. The equilibrium contact angle for a yield-stress fluid droplet has been measured and reported by German and Bertola [19], but it was not informed in the literature of Saïdi et al. [20]. If an accurate equilibrium contact angle for a yield-stress fluid were available from experiments of Saïdi et al. [20], more accurate numerical results could be expected.

Fig. 2a shows that, for identical fluid properties, both the spreading and retraction became weaker with decreasing impact velocity. The numerical results also showed the complete inhibition of retraction at an impact velocity of 0.6 m s^{-1} , consistent with the experimental results. Fig. 2b shows that the spreading and retraction became weaker with increasing yield-stress magnitude for an identical impact velocity.

The droplet impact dynamics of a yield-stress fluid exhibit some distinct characteristics. In Fig. 2, the time scale of the spreading phase is of the order of 1 ms, while the time scale to reach the final sessile state is of the order of 100 ms. In addition, the retraction rate decreases continuously as the droplet reaches the final sessile state. Fig. 3 shows the evolution of the droplet shape after impacting on the substrate for validation case 4, and also the apparent viscosity distributions and velocity vectors. It can be noted here that shear-thinning fluids exhibit high apparent viscosities at low shear rate and low apparent viscosities at high shear rate. During the impact process, the apparent viscosity of the fluids varies spatially and temporally, as shown in Fig. 3. Spatially, a high apparent viscosity appears at the bottom center region of the droplet, where the flow field stagnates, and a low apparent viscosity appears near the contact line due to a high shear rate. Temporally, the droplet becomes more viscous as it reaches its final sessile state. An increase in the apparent viscosity over time may explain the slowing of the retraction rate and the much longer time scale to reach the final sessile state. For more detailed analysis, the contact line velocity was calculated from the time derivative of the radius of the wetted area as follows:

$$V_{cl} = \frac{dR}{dt} \quad (18)$$

where R is the radius of the wetted area and V_{cl} is the contact line velocity. Fig. 4 shows the time evolution of contact line velocity for validation case 4. Contact line velocities were significantly higher than the impact speed in the initial stage of drop spreading. In contrast, contact line velocities during the relaxation phase were approximately two orders of magnitude lower than during the spreading phase, confirming the very slow rate of retraction appearing in Fig. 2. This also indicates that the dynamics during the spreading phase are mainly determined by the inertial effects, while the inertial effects are not important during the relaxation phase.

3.2. Spreading phase

In the experiments of Saïdi et al. [20], the spreading rate and the maximum spreading parameter tend to decrease as the concentration of gel increases. The real rheological parameters of fluids and the measured maximum spreading parameter at $V_0 = 3 \text{ m s}^{-1}$ in the experiments of Saïdi et al. are listed in Table 2, where the concentration increases from Gel 1 to Gel 7. Among the three rheological parameters, τ_0 represents yield-stress effects, while K and n are relevant to viscous effects. When the gel concentration increases, τ_0 and K increase, resulting in an increase in the resisting force to spreading, and this could be responsible for the decrease in the maximum spreading parameter. In contrast, n decreases as the gel concentration increases, resulting in more shear-thinning behavior. As n decreases, we expect an increase in the maximum spreading parameter due to lower apparent viscosities during inertial expansion [18]. However, it is difficult to quantify the independent influence of τ_0 , K , and n on the impact dynamics by direct experimental comparison, because the rheological parameters cannot be controlled separately in the experiments. We controlled the rheological parameters separately in our numerical simulation method with the aim of revealing which rheological parameter, among τ_0 , K , and n , induces the decrease in the maximum spreading parameter as the concentration increases.

At first, we used Gel 3 as a reference case, changing τ_0 between 0.14, 5.8, 21.1, and 34.3 Pa, while keeping the values of K and n constant ($K = 3 \text{ Pa s}^n$, $n = 0.42$), to reveal the independent influence of τ_0 on the spreading phase. Despite the different values of τ_0 , the time evolution of the spreading parameter was similar during the spreading phase, as shown in Fig. 5a, indicating that τ_0 has a negligible effect on the spreading phase. In the numerical experiments, high Re_n (>100) and We (>200) values mean that inertial effects are at least two orders of magnitude larger than both the viscous and the capillary effects. High Ca_n (>1) and low Bi (<1) values mean that viscous effects prevailed over both the capillary effects and the yield-stress effects, and low \hat{B} (<1) means that capillary effects prevailed over yield-stress effects. Therefore, the most dominant factor was inertial effects and the least significant factor was yield-stress effects, which could explain the negligible effect of τ_0 on the spreading phase. This suggests that the weakening of the spreading as the concentration increases did not arise from the increase in τ_0 .

In the second numerical simulation set, we changed K between 0.5, 3.0, 9.1, and 12.8 Pa s^n , while keeping the values of τ_0 and n constant ($\tau_0 = 5.8 \text{ Pa}$, $n = 0.42$), to reveal the independent influence of K on the spreading phase. An increase in K resulted in an increase in the viscous effects, and therefore led to a decrease in the spreading rate and the maximum spreading parameter, as shown in Fig. 5b. This result shows a similar trend to the experiments of Saïdi et al. [20], where the maximum spreading parameter decreased with an increase in K . We then changed n between 0.47, 0.42, and 0.35, while keeping the values of τ_0 and K constant ($\tau_0 = 5.8 \text{ Pa}$, $K = 3.0$), to reveal the independent influence of n on the spreading phase. Fig. 5c shows that a decrease in n results in an increase in the spreading rate and the maximum spreading parameter. This is because a decrease in n results in a decrease in the apparent (effective) viscosity [27]. This result shows the opposite trend to the experiments of Saïdi et al. [20], where the maximum spreading parameter decreased with a decrease in n . This finding suggests that while both K and n affect the spreading phase, the spreading behavior is mainly determined by the value of K . In conclusion, the experimentally observed weakening of spreading as the gel concentration increases is irrespective of any increase in τ_0 , instead arising from an increase in K that is slightly compensated by a decrease in n .

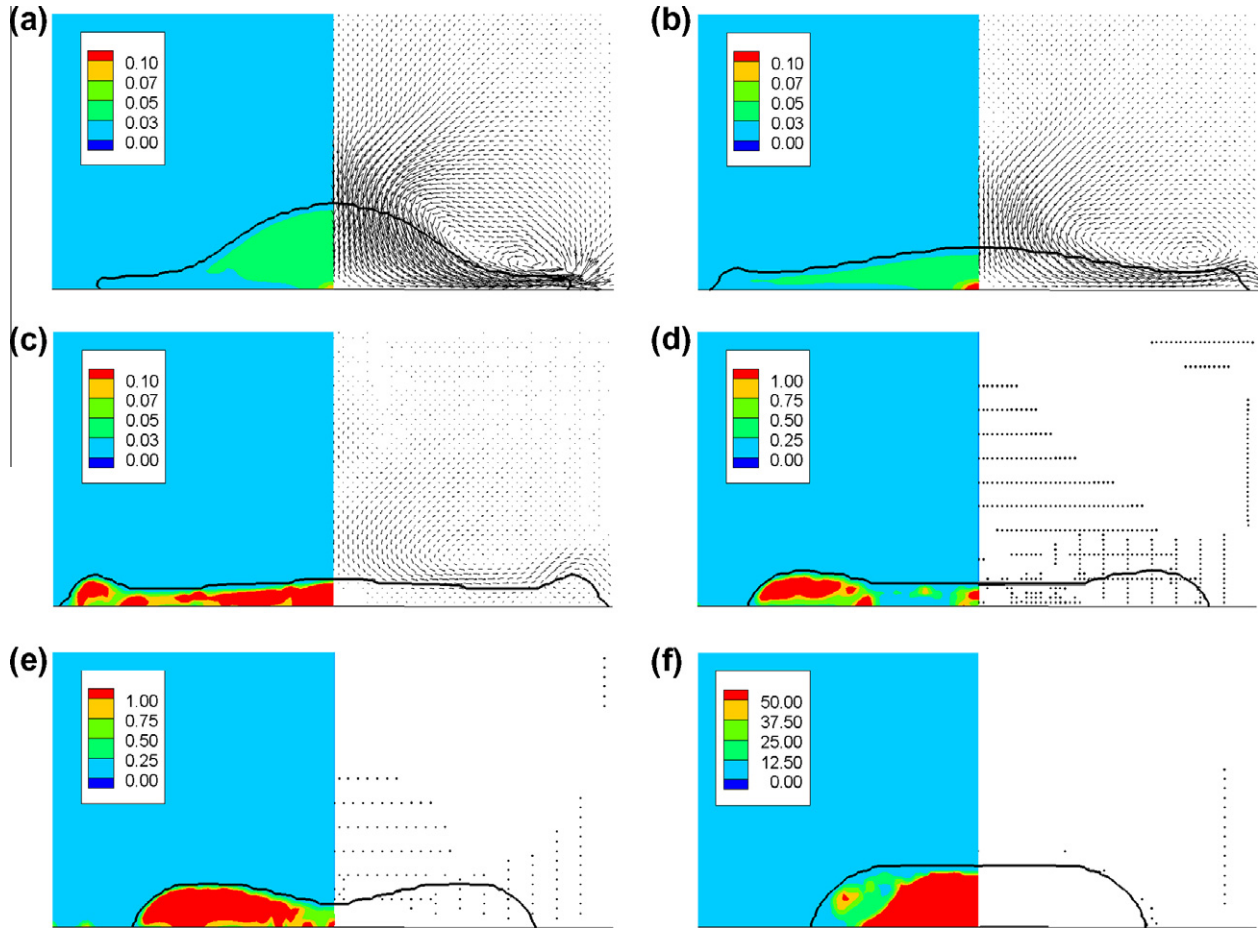


Fig. 3. Time evolution of the droplet shape for case 4. The apparent viscosity ($\text{kg m}^{-1} \text{s}^{-1}$) distributions are plotted on the left, and the velocity vectors on the right. (a) $t = 0.46$, (b) $t = 0.83$, (c) $t = 1.6$, (d) $t = 28.4$, (e) $t = 90.3$, and (f) $t = 474$ ms.

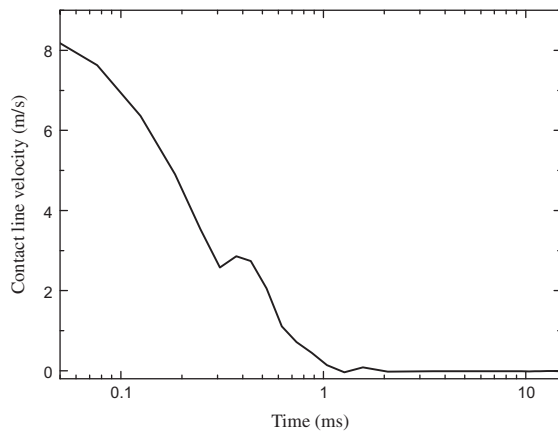


Fig. 4. Time evolution of contact line velocity for case 4.

Table 2
Rheological parameters of fluids and measured maximum spreading parameter at $V_0 = 3 \text{ m s}^{-1}$ in the experiments [20].

	τ_0 (Pa)	K (Pa s^n)	n	D_{max}/D_0
Gel 1	0.14	0.5	0.47	3.1
Gel 3	5.8	3	0.42	2.5
Gel 5	21.1	9.1	0.34	2.2
Gel 7	34.3	12.8	0.35	1.8

Fig. 10 illustrates the influence of surface tension during the spreading phase. The influence of surface tension was negligible in the initial stage of spreading, but became important at a later stage. An increase in the surface tension results in a decrease in the extent of spreading.

To characterize the dynamics during the spreading phase, we compared the relative importance of four effects: inertial, capillary, viscous, and yield-stress effects. When $We > 1$, indicating inertia-driven spreading, the spreading phase is governed by the ratio of the driving force (inertial force) to the resisting force (surface tension force, viscous force, and yield-stress). Because the yield-stress negligibly affected the spreading phase, as shown in Fig. 5a, the spreading phase could be described by the relative importance of inertial, surface tension, and viscous forces. Therefore, the dynamics during the spreading phase could be characterized by Re_n and We , which represent the ratios of inertial to viscous and inertial to surface tension forces, respectively.

In the case of Newtonian droplet impact, the maximum spreading parameter is predicted to scale as $D_m/D_0 \sim Re^{1/5}$, where $Re = \rho V_0 D_0 / \mu$ (μ is the fluid viscosity), based on the assumption that all of the initial kinetic energy is dissipated by viscosity [3,39]. Luu and Forterre [17] modified the scaling law with respect to shear-rate dependent viscosity of yield-stress fluid. Assuming $\mu = K \dot{\gamma}^{n-1} \sim K(V_0/h)^{n-1}$, where h is the thickness at the maximum spreading, and using volume conservation ($D_0^3 \sim h D_{\text{max}}^2$) yields $D_{\text{max}}/D_0 \sim Re_n^{1/(2n+3)}$. For low Bi number ($Bi < 0.5$), which indicates small effects of yield stress compared to viscous effects, their experimental data well followed the scaling law. Their prediction

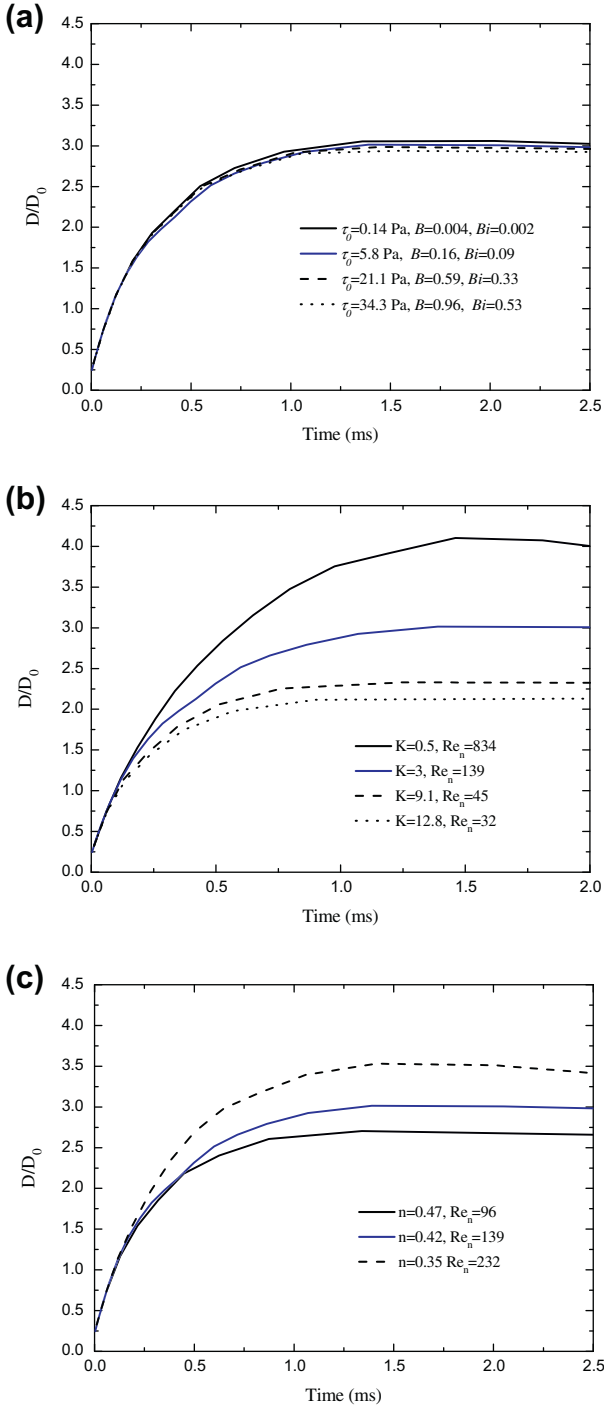


Fig. 5. Time evolution of the spreading parameter during the spreading phase, demonstrating the influence of rheological parameters on the spreading phase for $V_0 = 3 \text{ m s}^{-1}$ and $We = 253$. The blue solid line represents a reference case, which is Gel 3 in Table 2. (a) Influence of τ_0 (Pa) when $K = 3.0$ (Pa sⁿ), $n = 0.42$, $Re_n = 134$, and $Ca_n = 1.8$. (b) Influence of K when $\tau_0 = 5.8$ Pa and $n = 0.42$. (c) Influence of n when $\tau_0 = 5.8$ Pa and $K = 3.0$ Pa sⁿ. (For interpretation of the references to colour in this figure legend, the reader is referred to the web version of this article.)

suggests that both Re_n and n are important parameters in determining the maximum spreading parameter. In other words, if impact conditions have a different value of n at identical Re_n , the spreading behavior could be different. In this study, yield-stress effects were negligible in the spreading phase, as shown in Fig. 5a, but capillary effects were not negligible due to the small size of the droplet. Therefore, the effect of surface tension, which

is embedded in We , on the maximum spreading parameter should be considered. Based on the assumption that all the initial kinetic energy is transferred into surface energy [42], the maximum spreading parameter is predicted to scale as $D_m/D_0 \sim We^{1/2}$. Clanet et al. [43] showed experimentally that the maximum spreading parameter is predicted to scale as $D_m/D_0 \sim We^{1/4}$ in the limit of low viscosity and low wettability. They also proposed the transition between the capillary regime ($D_m/D_0 \sim We^{1/4}$) and viscous regime ($D_m/D_0 \sim Re_n^{1/5}$) based on the impact number $P \equiv We/Re_n^{4/5}$. In their experiments, the capillary regime was observed for small P ($P < 0.3$) and the viscous regime for larger P ($P > 50$). They suggested that the transition occurred around $P = 1$. To predict the maximum spreading parameter based on n , Re_n , and We , we performed extensive numerical simulations over the ranges $0.35 \leq n \leq 0.5$, $15 \leq Re_n \leq 230$, $28 \leq We \leq 400$, $1 \leq K \leq 9 \text{ Pa s}^n$, $1 \leq V_0 \leq 3 \text{ m s}^{-1}$, and $0.02 \leq \sigma \leq 0.071$ at fixed $\tau_0 = 5.8$ Pa. A few results are presented in Fig. 6. Fig. 6 shows that the maximum spreading diameter increases as Re_n increases when n and We are kept constant. The comparison of solid lines in Fig. 6 shows that a decrease in n induces an increase in the maximum spreading parameter at identical Re_n and We , because a decrease in n decreases the apparent (effective) viscosity [27]. When n and Re_n are kept constant, Fig. 10 shows that the spreading rate and the maximum spreading parameter tends to decrease with decreasing We , because a decrease in We means an increase in capillary effects, which act as the resisting force to spreading. Fig. 7a shows the maximum spreading parameter as a function of $Re_n^{1/(2n+3)}$, according to the prediction of Luu and Forterre [17], and also shows a dependence on We . The numerical results show a linear relationship between the maximum spreading parameter and $Re_n^{1/(2n+3)}$, supporting the prediction of Luu and Forterre [17]. In Fig. 7b, all the numerical data was fitted to a single scaling relation based on n , Re_n , and We giving the law $D_m/D_0 \sim Re_n^{1/(2n+3)} We^{0.0862}$. In the numerical simulations, the value of P was between 1.4 and 7.8, thus, it seems that the impact conditions can not be simply described by one of the two scaling law, for the capillary regime or for the viscous regime. It should be noted that the power law index 0.0862 is empirically determined fitting parameter. Experimentally determined maximum spreading parameters within the range $0.14 \leq \tau_0 \leq 28.3$ and for impact velocities of 2 and 3 m s^{-1} are also presented in Fig. 7b as a function of $Re_n^{1/(2n+3)} We^{0.0862}$, and they show a linear relationship with the proposed scaling parameter. However, the fitting curve for numerical and experimental data do not collapse on the same curve, which may be due to different contact angle conditions and the tendency to overpredict the maximum spreading diameter in the numerical simulation. The proposed prediction of the maximum spreading parameter will be useful in the design and optimization of spray coating, inkjet printing processes, or direct ink writing of complex 3D structures when yield-stress fluids are used as the working fluid.

3.3. Relaxation phase

After the droplet reaches its maximum spread, surface tension induces retraction when a droplet impacts on a partially wetting surface. During the retraction process, the surface energy is reversely transferred to inertial energy or viscous energy dissipation.

The numerical results shown in Fig. 8 are identical to those in Fig. 5a, but are plotted up to 250 ms in order to demonstrate the influence of τ_0 on the relaxation phase. It is apparent that by increasing τ_0 while keeping K and n constant, the retraction becomes slower. Unlike the spreading phase, where the influence of τ_0 was negligible, τ_0 had a critical influence on the retraction rate. This could be explained by the fact that the relative importance of yield-stress effects increased, while the relative importance of inertial and viscous effects decreased due to the very

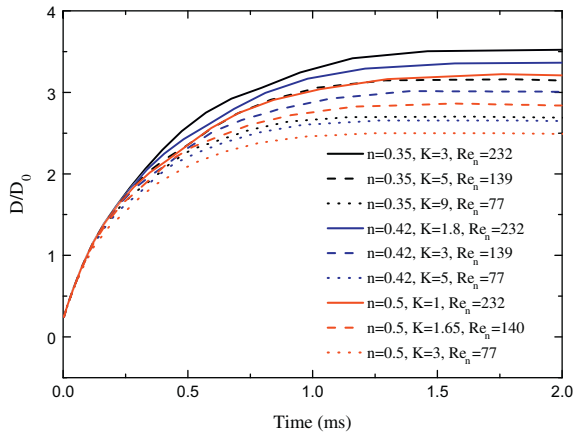


Fig. 6. Time evolution of the spreading parameter during the spreading phase, demonstrating the influence of n and Re_n when $\tau_0 = 5.8$ Pa, $V_0 = 3$ m s⁻¹ and $We = 253$.

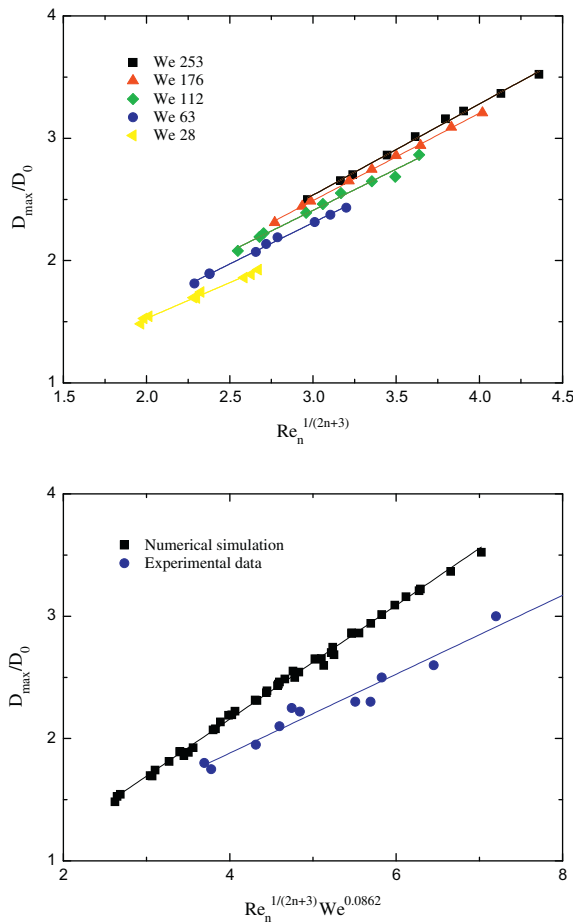


Fig. 7. (a) Plot of maximum spreading parameter as a function of $Re_n^{1/(2n+3)}$ at different We values. (b) Best fit to the present numerical simulation data showing the relationship between the maximum spreading parameter and n , Re_n , and We giving the law $D_m D_0 \sim We^{0.0862} Re_n^{1/(2n+3)}$. The experimental data is from Saïdi et al. [20].

small magnitude of velocity during the relaxation phase. In order to compare the relative importance of four effects (inertia, capillary, viscous, and yield-stress effects) during the retraction process, the retraction velocity V_{ret} ($=dR/dr$) was obtained using linear fitting of the retraction curves in Fig. 8, and we present the magnitude of four forces based on the retraction velocity in Table 3.

Typically, capillary effects were the single most dominant factor governing the retraction process. At relatively small yield-stress magnitudes for $\tau_0 = 0.14$ and $\tau_0 = 5.8$ Pa, the yield-stress effects were still minor factors, and the numerical results of two impact conditions showed similar retraction curves, as shown in Fig. 8, despite the different yield-stress magnitude. However, at relatively large yield-stress magnitudes for $\tau_0 = 21.1$ and $\tau_0 = 34.3$ Pa, the yield-stress effects were the second most important factor, and the numerical results of two impact conditions showed apparently different retraction curves depending on the value of τ_0 .

Fig. 9a shows the influence of K and n at fixed values of $\tau_0 = 5.8$ Pa and $V_0 = 2$ m s⁻¹. Numerical results show that an increase in K results in a slower retraction at a fixed τ_0 and n . An increase in K has two distinct effects on the retraction: it weakens the driving force and strengthens the resisting force. The driving force is weakened because an increase in K results in a smaller maximum spreading diameter due to higher viscosities during the spreading phase, indicating that the surface energy at the maximum spreading, which induces retraction, is smaller. The resisting force is strengthened because an increase in K results in higher viscosities during the retraction phase. These combined factors contribute to the weaker retraction as K increases. Similarly, an increase in n results in a slower retraction at a fixed τ_0 and K in the same manner as the increase in K .

The numerical results shown in Fig. 10 are identical to those in Fig. 6b, but are plotted up to 100 ms in order to demonstrate the influence of σ on the relaxation phase. As σ increases, retraction becomes stronger because surface tension forces act as driving forces to the retraction. As shown, the influence of σ was more noticeable in the retraction process than in the spreading phase. This is due to the fact that the capillary effects are the most dominant factor governing the relaxation phase, as described before, and consequently the numerical results show apparently different retraction curves depending on the value of σ .

As previously mentioned, during the relaxation phase inertia effects were negligible and the capillary, viscous, and yield-stress effects were important, so that yield-stress effects are included and inertial effects are excluded when characterizing the dynamics. Therefore, the three important effects governing the relaxation phase are capillary, viscous, and yield stress effects. The relaxation phase is governed by the ratio of the driving force (surface tension force) to the resisting force (viscous force and yield-stress). The appropriate non-dimensional parameter used to characterize the retraction phase could be Ca_n and \tilde{B} , which represent the ratios

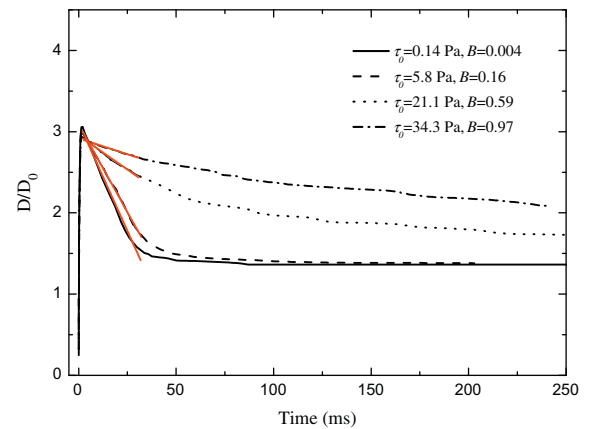


Fig. 8. Time evolution of the spreading parameter demonstrating the influence of τ_0 (Pa) on the relaxation phase when $V_0 = 3$ m s⁻¹, $K = 3.0$ Pa sⁿ, $n = 0.42$, $Re_n = 134$, $We = 253$ and $Ca_n = 1.82$. The red solid lines are linear fits to retraction curves. (For interpretation of the references to color in this figure legend, the reader is referred to the web version of this article.)

Table 3
Retraction velocity, V_{ret} ($=dR/dt$), which was obtained by linear fitting to retraction curves in Fig. 8, and comparison of relative importance of four effects based on the receding velocity. K and n were kept constant ($K = 3 \text{ Pa s}^n$, $n = 0.42$) and $V_0 = 3 \text{ m s}^{-1}$.

	Retraction velocity V_{ret} (m/s)	Inertia effects (ρV_{ret}^2)	Capillary effects (σ/D_0)	Viscous effects (kV_{ret}^n/D_0^n)	Yield-stress effects (τ_0)
$\tau_0 = 0.14 \text{ Pa}$	0.053	2.8	35.5	11.9	0.14
$\tau_0 = 5.8 \text{ Pa}$	0.043	1.8	35.5	10.9	5.8
$\tau_0 = 21.1 \text{ Pa}$	0.017	0.3	35.5	7.4	21.1
$\tau_0 = 34.3 \text{ Pa}$	0.008	0.06	35.5	5.3	34.4

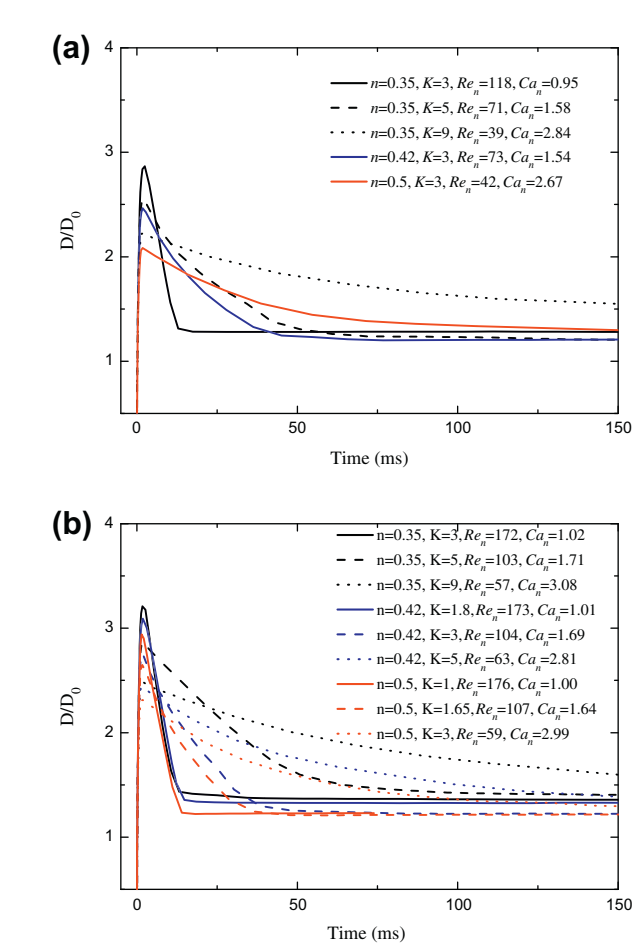


Fig. 9. Time evolution of the spreading parameter demonstrating the influence of n and K (Pa s^n) on the relaxation phase. (a) $\tau_0 = 5.8 \text{ Pa}$, $V_0 = 2 \text{ m s}^{-1}$, $We = 112$ and $\hat{B} = 0.16$. (b) $\tau_0 = 5.8 \text{ Pa}$, $V_0 = 2.5 \text{ m s}^{-1}$, $We = 176$ and $\hat{B} = 0.16$.

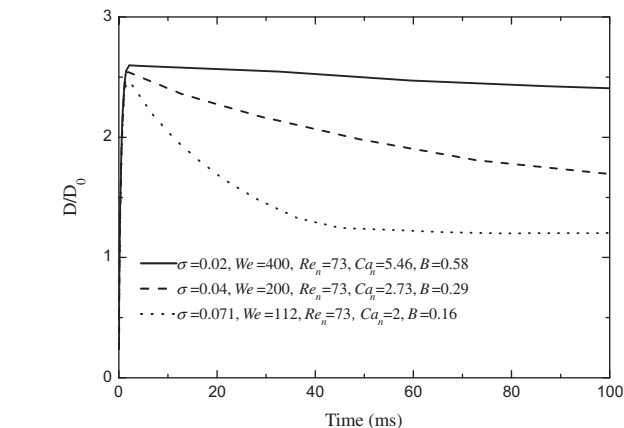


Fig. 10. Time evolution of the spreading parameter demonstrating the influence of σ (N m^{-1}) at fixed $\tau_0 = 5.8 \text{ Pa}$, $K = 3.0 \text{ Pa s}^n$, $n = 0.42$, and $V_0 = 2 \text{ m s}^{-1}$.

of viscous to capillary and yield stress to capillary effects, respectively. When the value of Ca_n is fixed, the retraction rate decreases as \hat{B} increases as shown in Fig. 8 because an increase in \hat{B} indicates an increase in resistance. When the value of \hat{B} is fixed, the retraction is fairly dependent on Ca_n in such a way that a droplet with a larger Ca_n value retracts slower. Moreover, a similar value of Ca_n shows the similar slope in the retraction curves, irrespective of the magnitude of the maximum spreading parameter, as shown in Fig. 9.

4. Conclusions

In this paper, presented is a numerical study on the impact dynamics of a yield-stress fluid droplet on a solid surface. The numerical simulation accounts for the yield-stress and shear-rate dependent viscosity using the Herschel–Bulkley model. The numerical results were compared to the experimental results showing a qualitative agreement. The numerical simulation on the droplet impact dynamics of yield-stress fluids was performed and lead to the following conclusions.

During the impact process, spatially and temporally varying viscosities were observed. Spatially, a high apparent viscosity appears at the bottom center region of the droplet, while a low apparent viscosity appears near the contact line. Temporally, the droplet becomes more viscous over time, resulting in a slowing of the retraction rate and a much longer time to reach the final sessile state.

During the spreading phase, the independent influence of the rheological parameters τ_0 , K , and n was investigated. An increase in τ_0 , while holding K and n constant, did not affect the spreading phase. An increase in K at a fixed τ_0 and n weakened the spreading, as did an increase in n at a fixed τ_0 and K . In addition, the influence of surface tension was investigated by varying the magnitude of σ . An increase in σ resulted in weaker spreading. Through extensive numerical simulations, the non-dimensional parameters n , Re_n , and We are determined to govern the spreading phase. An increase in Re_n and We resulted in a larger spreading rate and extent, while an increase in n resulted in weaker spreading. Furthermore, it is found that the maximum spreading parameter scales as $D_m/D_0 \sim Re_n^{1/(2n+3)} We^{0.0862}$.

During the relaxation phase, the independent influence of the rheological parameters τ_0 , K , and n was also investigated. An increase in τ_0 while holding K and n constant dampened the retraction. An increase in K at a fixed n and τ_0 weakened the retraction, as did an increase in n at a fixed K and τ_0 . In addition, a decrease in σ resulted in weaker retraction. The non-dimensional parameters governing the retraction were found to be the Ca_n and the \hat{B} number. A decrease in Ca_n and \hat{B} resulted in faster retraction.

In summary, the value of K and n affected the entire impact process, as an increase in K and n weakened both spreading and retraction. τ_0 did not affect the spreading phase, but affected the retraction process in such a manner that an increase in τ_0 weakened retraction. An increase in σ weakened spreading but strengthened the retraction.

References

- [1] R. Rioboo, M. Marengo, C. Tropea, Time evolution of liquid drop impact onto solid, dry surfaces, *Exp. Fluids* 33 (2002) 112–114.

- [2] J. Fukai, Z. Zhao, D. Poulikakos, C.M. Megaridis, O. Miyatake, Modeling of the deformation of a liquid droplet impinging upon a flat surface, *Phys. Fluids A* 5 (1993) 2588–2599.
- [3] M. Rein, Phenomena of liquid drop impact on solid and liquid surfaces, *Fluid Dyn. Res.* 12 (1993) 61–93.
- [4] M. Pasandideh-Fard, Y.M. Qiao, S. Chandra, J. Mostaghimi, Capillary effects during droplet impact on a solid surface, *Phys. Fluids* 8 (1995) 650–659.
- [5] T. Mao, D.C.S. Kuhn, H. Tran, Spread and rebound of liquid droplets upon impact on flat surfaces, *AIChE J.* 43 (1997) 2169–2179.
- [6] M. Bussmann, S. Chandra, J. Mostaghimi, Modeling the splash of a droplet impacting a solid surface, *Phys. Fluids* 12 (2000) 3121–3132.
- [7] H.Y. Kim, J.H. Chun, The recoiling of liquid droplets upon collision with solid surfaces, *Phys. Fluids* 13 (2001) 643–645.
- [8] Š. Šikalo, M. Marengo, C. Tropea, E.N. Ganic, Analysis of droplet impact on horizontal surfaces, *Exp. Therm. Fluid Sci.* 25 (2002) 503.
- [9] I.V. Roisman, R. Rioboo, C. Tropea, Normal impact of a liquid drop on dry surface. model for spreading and receding, *Proc. Roy. Soc. Lond. A* 458 (2002) 1411–1430.
- [10] Š. Šikalo, H.D. Wilhelm, I.V. Roisman, S. Jakirlic, C. Tropea, Dynamic contact angle of spreading droplets: experiments and simulations, *Phys. Fluids* 17 (2005) 062103.
- [11] A.L. Yarin, Drop impact dynamics: splashing, spreading, receding, bouncing, *Annu. Rev. Fluid Mech.* 38 (2006) 159–192.
- [12] S.F. Lunkad, V.V. Buwa, K.D.P. Nigam, Numerical simulations of drop impact and spreading on horizontal and inclined surfaces, *Chem. Eng. Sci.* 62 (2007) 7214–7224.
- [13] P. Attané, F. Girard, V. Morin, An energy balance approach of the dynamics of drop impact on a solid surface, *Phys. Fluids* 19 (2007) 012101.
- [14] G. German, V. Bertola, Review of drop impact models and validation with high-viscosity Newtonian fluids, *Atomization Sprays* 19 (2009) 787–807.
- [15] J.A. Lewis, Direct ink writing of 3D functional materials, *Adv. Funct. Mater.* 16 (2006) 2193–2204.
- [16] S. Nigen, Experimental investigation of the impact of an (apparent) yield-stress material, *Atomization Sprays* 15 (2005) 103–117.
- [17] L.H. Luu, Y. Forterre, Drop impact of yield-stress fluids, *J. Fluid Mech.* 632 (2009) 301–327.
- [18] G. German, V. Bertola, Impact of shear-thinning and yield-stress drops on solid substrates, *J. Phys.: Condens. Matter* 21 (2009) 375111.
- [19] G. German, V. Bertola, The spreading behaviour of capillary driven yield-stress drops, *Colloids Surfaces A: Physicochem. Eng. Aspects* 366 (2010) 18–26.
- [20] A. Saïdi, C. Martin, A. Magnin, Influence of yield-stress on the fluid droplet impact control, *J. Non-Newton. Fluid Mech.* 165 (2010) 596–606.
- [21] S. Schiaffino, A.A. Sonin, Molten droplet deposition and solidification at low Weber numbers, *Phys. Fluids* 9 (1997) 3172–3187.
- [22] G. German, V. Bertola, The free-fall of viscoplastic drops, *J. Non-Newton. Fluid Mech.* 165 (2010) 825–828.
- [23] A. Saïdi, C. Martin, A. Magnin, Effects of surface properties on the impact process of a yield stress fluid drop, *Exp. Fluids* (2011) 1–14.
- [24] P. Jay, A. Magnin, J.M. Piau, Viscoplastic fluid flow through a sudden axisymmetric expansion, *AIChE J.* 47 (2001) 2155–2161.
- [25] C.W. Hirt, B.D. Nichols, Volume of fluid (VOF) method for the dynamics of free boundaries, *J. Comput. Phys.* 39 (1981) 201–225.
- [26] J.U. Brackbill, D.B. Kothe, C. Zemach, A continuum method for modeling surface tension, *J. Comput. Phys.* 100 (1992) 335–354.
- [27] A. Dechelette, P.E. Sojka, C.R. Wassgren, Non-Newtonian drops spreading on a flat surface, *J. Fluids Eng.* 132 (2010) 101301–101302.
- [28] E.J. O'Donovan, R.I. Tanner, Numerical study of the Bingham squeeze film problem, *J. Non-Newton. Fluid Mech.* 15 (1984) 75.
- [29] G.R. Burgos, A.N. Alexandrou, On the determination of yield surfaces in Herschel–Bulkley fluids, *J. Rheol.* 43 (1999) 463.
- [30] V. Bertola, Wicking with a yield-stress fluid, *J. Phys.: Condens. Matter* 21 (2009) 035107.
- [31] S.F. Kistler, L.E. Scriven, Coating flow theory by finite element and asymptotic analysis of the Navier–Stokes system, *Int. J. Numer. Methods Fluids* 4 (1984) 207–229.
- [32] E. Mitsoulis, Numerical simulation of calendaring viscoplastic fluids, *J. Non-Newton. Fluid Mech.* 154 (2008) 77–88.
- [33] J. Fukai, Y. Shiiba, T. Yamamoto, O. Miyatake, D. Poulikakos, C.M. Megaridis, Z. Zhao, Wetting effects on the spreading of a liquid droplet colliding with a flat surface. Experiment and modeling, *Phys. Fluids* 7 (1995) 236.
- [34] H. Liu, S. Krishnan, S. Marella, H.S. Udaykumar, Sharp interface Cartesian grid method II: a technique for simulating droplet interactions with surfaces of arbitrary shape, *J. Comput. Phys.* 210 (2005) 32–54.
- [35] S. Shin, D. Juric, Simulation of droplet impact on a solid surface using the level contour reconstruction method, *J. Mech. Sci. Technol.* 23 (2009) 2434–2443.
- [36] D.B. van Dam, C.L. Clerc, Experimental study of the impact of an ink-jet printed droplet on a solid substrate, *Phys. Fluids* 16 (2004) 3403.
- [37] H. Dong, W.W. Carr, D.G. Bucknall, J.F. Morris, Temporally-resolved inkjet drop impact on surfaces, *AIChE J.* 53 (2007) 2606–2617.
- [38] S. Chandra, C.T. Avedisian, On the collision of a droplet with a solid surface, *Proc. Roy. Soc. Lond. A* 432 (1991) 13–41.
- [39] D.J.E. Harvie, M.R. Davidson, M. Rudman, An analysis of parasitic current generation in volume of fluid simulations, *ANZIAM J.* 46E (2005) 133–149.
- [40] S. Popinet, An accurate adaptive solver for surface-tension-driven interfacial flows, *J. Comput. Phys.* (2009) 5838–5866.
- [41] D. Richard, C. Clanet, D. Quéré, Surface phenomena: contact time of a bounding drop, *Nature* 417 (2002) 811.
- [42] C. Clanet, C. Béguin, D. Richard, D. Quéré, Maximal deformation of an impacting drop, *J. Fluid Mech.* 517 (2004) 199–208.